Fabrication of 3D mesoporous networks of assembled CoO nanoparticles for efficient photocatalytic reduction of aqueous Cr(VI)

Georgia Velegraki[a], Jianwei Miao[b], Charalampos Drivas[c], Bin Liu[b], Stella Kennou[c], Gerasimos S. Armatas[a],[*]

[a] University of Crete, Department of Materials Science and Technology, Heraklion 71003, Greece
[b] Nanyang Technological University, School of Chemical and Biomedical Engineering, 62 Nanyang Drive, Singapore 637459, Singapore
[c] University of Patras, Department of Chemical Engineering, Patra 26504, Greece

ARTICLE INFO

ABSTRACT

Synthesis of high-performance and cyclic stable photocatalysts has been remaining a significant challenge. In this work, we report the synthesis of high-surface-area mesoporous networks of CoO NPs through a polymer-templating self-assembly method and demonstrate their potential application in the reductive detoxification of aqueous Cr(VI) solutions under UV and visible light irradiation. Electron microscopy images and N_2 adsorption measurements corroborate the presence of a porous network of interconnected CoO NPs (ca. 18 nm in size) with large internal surface area (up to 134 $m^2\,g^{-1}$) and narrow pore-size distribution (ca. 4.4–4.8 nm in diameter). Conjunction of optical absorption and electrochemical impendence spectroscopy results indicates that the band edge positions of constituent CoO NPs meet the electric potential requirements for reducing Cr(VI) and splitting water to oxygen. We show that mesoporous assemblies of hexagonal CoO NPs effectively overcome the kinetic barriers for the oxidation reaction, manifesting a remarkably photocatalytic Cr(VI) reduction activity at acidic pH with an apparent quantum yield (AQY) of 1.61% and 0.17% at wavelengths of 375 and 440 nm, respectively. We demonstrate that, apart from oxygen evolution reaction, photoconversion of harmful Cr(VI) into non-toxic Cr(III) involves also a hydroxyl radical-mediated oxidation process by intercepting oxidation products with on-line mass spectrometry and fluorescence spectroscopy in control catalytic experiments.

1. Introduction

Hexavalent chromium (Cr(VI)) represents a serious environmental pollution problem that is arising from various industrial activities such as electroplating, leather tanning, paint and pigments among others [1]. Cr(VI) is highly toxic to human health, and has been classified as carcinogen and mutagen by the International Agency for Research on Cancer (IARC) with LD50 values between 50 and 150 mg kg^{-1} [2,3]. Because of its non-biodegradable nature, Cr(VI) can contaminate groundwater and shallow water wells with detrimental effects to the environment [4]. Hence, many countries regulate its allowable limit concentration in drinking water. For example, US Environmental Protection Agency (EPA) has set the maximum contaminant level for total chromium in drinking water to be 0.1 mg L^{-1} [5]. Consequently, the effective and sustainable detoxification of Cr(VI)-bearing aqueous solutions is one of the high-priority research directions.

To date, a variety of techniques such adsorption, ion-exchange, chemical precipitation, and biological, chemical and electrochemical reduction have been proposed for detoxification of aqueous Cr(VI) solutions [6–8]. Nevertheless, although successful, these techniques are costly, complicated, and require lengthy processing times. Alternatively, the photocatalytic reduction of Cr(VI) to Cr(III) over a semiconductor photocatalyst has been considered as a promising means for effective and sustainable detoxification of Cr(VI)-bearing solutions. The Cr(III) is about 100–1000 times less toxic than Cr(VI) and can be easily removed from the solution as Cr_2O_3 or $Cr(OH)_3$ precipitates in alkaline conditions [9]. Therefore, in recent years, researchers strive to neutralize the deteriorating effects of Cr(VI) to less nocuous Cr(III) form by photocatalytic reduction [10].

So far, though many materials have been investigated as potential photocatalysts for Cr(VI) reduction (such as TiO_2 [11,12], $Bi_{24}O_{31}Br_{10}$ [13], $NaTaO_3$ [14], SnS_2 [15], Ag_2S/Ag [16], CdS [17], $(AgIn)_xZn_{2(1-x)}S_2$ [18], g-C_3N_4 [19]), their efficiency and cyclic stability are still not suitable for commercial applications. These materials generally suffer from one or more drawbacks such as poor utilization of solar energy due to their large band gap (> 2.8 eV), low electrical conductivity,

short lifetime of photogenerated electron-hole pairs, and anodic photocorrosion of the crystal lattice. Furthermore, most of these catalysts, although have good water oxidation potential, operate in the presence of hole sacrificial reagents such as ascorbic acid, ethylenediaminetetraacetic acid (EDTA), formic acid and ammonium ions, which are essential to trigger Cr(VI) photoreduction [20]. In general, the photooxidation of water to dioxygen is a sluggish reaction that involves several uphill reaction steps such as dissociation of OH− species and formation of O−O bonds [21]. Therefore, the development of a stable and efficient photocatalyst for the simultaneous Cr(VI) reduction and water oxidation in aqueous solutions is of particular interest because of the simplicity and low cost of operation.

Cobalt monoxide (CoO) is an interesting semiconductor material with an energy band gap of 2.4–2.7 eV [22]. It crystalizes in two structures, the cubic rocksalt and the hexagonal wurtzite phase. Although cubic close-packed structure is thermodynamically more stable, the hexagonal form of CoO displays interesting electrical, optical, magnetic, and electrochemical properties [23,24] that are useful for a variety of potential applications such as catalysis, gas sensors, magnetic data storage devices and lithium-ion batteries [25,26]. Meanwhile, currently the fabrication of CoO materials at the nanoscale has been the subject of extensive research in photoelectrochemical cells and magnetic nanodevices [27]. For instance, recently Liao et al. designed CoO nanoparticles (NPs) with tunable band-edge positions and demonstrated their high activity for photocatalytic water splitting [28].

We recently demonstrated a solution phase self-assembly of colloidal NP building blocks with soft templates such as amphiphilic block-copolymers to prepare three-dimensional (3D) mesoporous networks [29]. In this approach, the inorganic NPs undergo evaporation-induced self-assembly with the polymer templates to produce hybrid organic-inorganic composites. The template can subsequently thermally decompose to yield a NP-linked mesoporous framework with open and interconnected porosity. Interestingly, these materials combine the unique catalytic and quantum-confined optical absorption properties of the precursor NPs with the large surface area of the porous structure. Furthermore, the very small size of the constituent NPs improves the charge separation and, thus, photocatalytic performance by providing short diffusion paths for electron transport. We showed that such a combination of complementary characteristics is beneficial for a range of catalytic reactions, such as oxidation of cyclic alkenes and aryl alkanes, reduction of aryl and alkyl nitro compounds and photocatalytic water splitting [30–33].

In this work, we report the synthesis of new mesoporous CoO materials from the polymer-assisted cross-linking of CoO NPs, and demonstrate for the first time the application of these single-component assemblies in photocatalytic reduction of aqueous Cr(VI) under UV and visible light irradiation. In general, the formation of a continuous network of connected NPs with open-pore structure is a challenging issue mainly because of the aggregation of NPs into large microstructures with limited porosity. The resulting assembled frameworks possess an inherently large pore surface, which provides a large number of exposed active sites for reactions. We show that mesoporous CoO NP networks can serve as an efficient catalyst to drive Cr(VI) reduction and water oxidation with high stability under UV and visible light irradiation. It is striking that the network structure of this material is quite stable under the reaction conditions and can undergo repeatable electrochemical redox transformations while preserving open porosity. Further, we suggest that, apart from reaction kinetics at the solid-liquid interface, morphological effects and crystal lattice reactivity might also contribute to the improved photocatalytic performance.

2. Experimental

2.1. Synthesis of CoO NPs

CoO NPs were prepared according to literature procedure [34].

Briefly, 1.5 mmol of Co(acac)$_3$ (98%, Sigma-Aldrich) and 300 mmol of oleylamine (70%, Sigma-Aldrich) were heated at 135 °C under inert atmosphere for 5 h. The resulting brown solution was then flash-heated to 200 °C and annealed for 3 h, giving a green suspension. Next, the supernatant was removed by centrifugation retrieving the CoO NPs in a powdery form. The CoO NPs were dispersed in hexane (95%, Sigma-Aldrich) to form a stable colloidal solution (10 mg mL^{-1}).

2.2. Ligand exchange of CoO NPs

The surface of CoO NPs was modified with NOBF$_4$ by a ligand-exchange process according to a previously reported method [35]. In detail, a dispersion of CoO NPs in hexane (6 mL) was added to a solution of NOBF$_4$ (60 mg, 97%, Acros Organics) in DMF (6 mL, 99.9%, Sigma-Aldrich) and the mixture was stirred at room temperature until the NPs were transferred to the DMF phase. The BF$_4$$^{-}$-capped CoO NPs were then collected by precipitation with toluene (99.7%, Sigma-Aldrich), followed by centrifugation. The ligand-stripped CoO NPs were dispersed in DMF to form a stable colloidal solution of 120 mg mL^{-1}.

2.3. Synthesis of CoO MNAs

For a typical synthesis of mesoporous CoO NP assemblies (CoO MNAs), 0.2 g of block copolymer Pluronic F127 (OH(CH$_2$CH$_2$O)$_{100}$(CH (CH$_3$)CH$_2$O)$_{64}$(CH$_2$CH$_2$O)$_{100}$H, M$_n$ ~ 12,000, Sigma-Aldrich) were dissolved in 1.5 mL of tetrahydrofuran (THF, > 99%, Sigma-Aldrich) with continuous stirring. To this solution, 0.5 mL of colloidal CoO NP solution in DMF was added dropwise and the mixture was stirred at room temperature for 2 h. Then, the resulting mixture was placed in an oven at 40 °C and left under static conditions for about 5–6 days to gives a mesostructured CoO/polymer composite. The resulting dry powder was subsequently heated to 350 °C for 4 h under N$_2$ flow (~50 cm^3 min^{-1}), using a heating rate of 1 °C min^{-1}, to yield the mesoporous product. For comparison, we also prepared random aggregates of CoO NPs (CoO RNAs) following a similar procedure to that of CoO MNAs, but in absence of template. Porous assemblies of Co$_3$O$_4$ NPs (Co$_3$O$_4$ MNAs) were also obtained by heating the CoO/polymer composite at 350 °C for 4 h in air.

2.4. Photocatalytic reactions

In a typical procedure, a quantity of catalyst (10–20 mg) was dispersed in 50 mL of 50 mg L^{-1} Cr(VI) aqueous solution, which were prepared by dissolving K$_2$Cr$_2$O$_7$ into deionized (DI) water. The pH of the solution was adjusted to the desired values with dilute sulfuric acid. Prior to irradiation, the suspension was magnetically stirred in the dark for 30 min to ensure equilibrium. The photoreduction reaction was performed by irradiating the solution with UV–vis or visible light, using a 300 W Xe lamp (Variac Cermax) with cut-off filters allowing λ > 360 nm or λ ≥ 420 nm, respectively. All the experiments were carried out at 20 ± 2 °C using a water bath cooling system. During reaction, the concentration of Cr(VI) in the solution was monitored *via* 1,5-diphenylcarbazide (DPC) colorimetric method, using a Perkin Elmer Lambda 25 UV–vis spectrometer. The normalized concentration (C/C$_o$) of Cr(VI) solution at different illumination times was calculated as proportional to the absorbance of the DPC–Cr(VI) complex at 540 nm (normalized to the initial absorption). Control experiments were carried out with the addition of phenol (10 equiv.) in the reaction mixture. Analysis of the reaction products was performed by extracting the organic compounds with ethyl acetate and then analyzing the extract by GC–MS (Shimadzu GCMS-QP2010 Ultra).

For the photooxidation of water to oxygen, 15 mg of CoO MNAs catalyst and 50 mL of 50 ppm Cr(VI) aqueous solution (pH = 2) were placed into a 100-mL airtight quartz tube. The temperature of the suspension was maintained at 20 ± 2 °C by using an external water cooling system. Prior irradiation, the mixture was purged with argon

for 30 min under atmospheric pressure to remove any dissolved air. The photocatalytic reaction took place under irradiation of a 300 W Xe lamp (λ > 360 nm). The oxygen generated from the reaction was analyzed with a gas chromatograph (Shimadzu GC-2014) equipped with a thermal conductivity detector.

The apparent quantum yield (AQY) of the catalyst was calculated by analyzing the amount of reduced Cr(VI) at a given monochromatic irradiation, using LED light with wavelengths of 375 and 440 nm, respectively:

$$AQY = \frac{3 \times \text{number of reduced Cr(VI)}}{\text{number of incident photons}} \quad (1)$$

The intensity of the incident light was measured using a StarLite energy meter equipped with a FL400A-BB-50 fan-cooled thermal sensor (Ophir Optronics Ltd, Jerusalem).

2.5. Physical characterization

Thermogravimetric analyses were performed using a Perkin Elmer Diamond analyzer. Thermal analysis was conducted from 40 to 600 °C in a nitrogen atmosphere (under a flow rate of ∼200 mL min^{-1}) with a heating rate of 5 °C min^{-1}. Powder X-ray diffraction (XRD) patterns were obtained with a PANalytical X'Pert Pro MPD X-ray diffractometer (45 kV and 40 mA) using Cu Kα radiation (λ = 1.5406 Å) in the Bragg–Brentano geometry. Transmission electron microscopy (TEM) images were taken with a JEOL JEM-2100 electron microscope, equipment with a LaB$_6$ filament, operating at 200 kV accelerating voltage. Samples were prepared by suspending fine powders in ethanol and then drop casting on a holey carbon-coated Cu grid. Nitrogen adsorption and desorption isotherms were measured at −196 °C on a Quantachrome NOVA 3200e sorption analyzer. Prior to measurement, samples were degassed at 100 °C under vacuum (< 10^{-5} Torr) for 12 h. The specific surface areas were calculated using the Brumauer-Emmett-Teller (BET) method [36] on the adsorption data in the relative pressure range of 0.05–0.22. The total pore volumes were estimated from the adsorbed amount at the relative pressure (P/P$_o$) of 0.98, and the pore size distributions were obtained from the adsorption branch of the isotherms, using the non-local density functional theory (NLDFT) method [37]. Diffuse reflectance UV–vis/near-IR spectra were collected using on a Perkin Elmer Lambda 950 optical spectrophotometer. BaSO$_4$ powder was used as a 100% reflectance standard and base material on which the powder sample was coated. Diffuse reflectance data were converted to absorption using the Kubelka-Munk function α/S = $(1 − R)^2/(2R)$, where R is the measured reflectance and α, S are the absorption and scattering coefficients, respectively [38]. The energy bandgap (E$_g$) of the samples were estimated from Tauc plots of $(\alpha h\nu)^2$ *versus* photon energy. Fluorescence spectra were obtained at room temperature on a Lumina Fluorescence spectrometer (Thermo scientific) equipped with a 150 W Xe lamp. X-ray photoelectron spectroscopy (XPS) measurements were carried out using a un-monochromatized Mg Kα line at 1253.6 eV (12 kV, 20 mA) and a Laybold EA-11 analyzer with pass energy of 100 eV, giving full width at half maximum (FWHM) of 1.3 eV for the Au 4f$_{7/2}$ peak. The binding energy scale was calibrated by hydrocarbon contamination using the C 1s peak at 284.8 eV.

2.6. Electrochemical measurements

Mott-Schottky plots were obtained with an electrochemical workstation (CHI 660E). A three-electrode set-up, with a platinum plate (1.0 × 2.0 cm^2) and a silver-silver chloride (Ag/AgCl, 3 M KCl) as the counter and reference electrodes, respectively, was adopted to study the samples. The capacitance of the semiconductor/electrolyte interface was collected at 1 kHz, with 10 mV AC voltage amplitude in 0.5 M Na$_2$SO$_4$ aqueous solution (pH = 7). Working electrode for impedance-potential measurements was fabricated as follows: ∼10 mg of CoO

catalyst was dispersed in 1 mL DI water and the mixture was subjected to sonication in a water bath until uniform suspension was formed. After that, 40 μL of the suspension were loaded on the surface of fluorine-doped tin oxide (FTO, 10 Ω/sq) substrate, which was masked using 3 M scotch tape with an effective area of 1 cm^2. The sample was dried in a 60 °C oven for 30 min.

3. Results and discussion

3.1. Synthesis and structural characterization

Mesoporous assemblies of CoO NPs (denoted as CoO MNAs) were successfully prepared by a polymer-assisted aggregating self-assembly method. In a typical synthesis, a colloidal dispersion of BF$_4^-$-stabilized CoO NPs in *N,N*-dimethylformamide (DMF) was added slowly to a solution of poly(ethylene oxide)-*b*-poly(propylene oxide)-*b*-poly(ethylene oxide) (F127) block copolymer (10 wt%) in THF. In the synthesis, we found that the concentration of CoO NPs and the evaporation rate of solvent are crucial parameters for obtaining assembled mesostructures with high porosity. Hence, optimal results were obtained using a F127/CoO/THF/DMF molar ratio of 0.02:1:23.12:8.1 and a slow evaporation of solvent (within ∼5–6 days, at 40 °C) in order the CoO NPs to co-assemble with the amphiphilic liquid-crystalline polymers and form mesostructured NP–F127 composites. This intermediate product was then calcined at 350 °C for 4 h in nitrogen to give an extended network of interconnected CoO NPs with accessible surface. The elimination of the polymer template was confirmed by thermogravimetric analysis (TGA). The TGA results of uncalcined CoO/polymer sample revealed a ∼82% of organic content incorporated between the framework (Fig. S1). After template-removal, no appreciable weight loss (less than 5%) was observed up to 480 °C, indicating that the polymer template is almost fully decomposed by 350 °C calcination; the weight loss (∼23%) observed in the 480–580 °C range is attributed to the reduction of CoO to Co under inert nitrogen atmosphere (see Fig. S2).

The crystallinity and phase purity of the porous framework were confirmed with X-ray diffraction (XRD), and typical result is shown in Fig. 1a. The XRD pattern of template-free CoO MNAs suggests the formation of a hexagonal lattice structure with *P*6$_3$*mc* symmetry, which is identical to that of the precursor NPs (Fig. S3). On the basis of the peak width of the (011) reflection and Scherrer's equation, the average domain size of the CoO crystallites in mesoporous CoO assemblies was estimated to be ∼18 nm, which is slightly larger than that of the precursor NPs (ca. 15 nm). This small increase is probably related to a low degree of interparticle fusion during the heating process.

Typical transmission electron microscopy (TEM) image of the mesoporous CoO assemblies is shown in Fig. 1b. It appears that the structure of CoO MNAs is actually constructed by numerous cross-linked NPs with an average diameter of 18 ± 5 nm (based on a count of more than 100 individual NPs, see inset of Fig. 1b), in good agreement with XRD results. High-resolution TEM (HRTEM) characterization reveals that the constituent NPs adopt a pyramid shape and exhibit single-crystal structure, displaying well-resolved lattice fringes throughout the particles, which, according to the fast Fourier transform (FFT) pattern, correspond to the (110) and (101) planes along the [111] zone axis of hexagonal CoO (Fig. 1c and inset). In addition, the HRTEM image shows intergrowth between neighboring NPs, suggesting the formation of a cross-linked NP network. Creating a continuous network of connected NPs is important for applications that require electronic connectivity and mechanical rigidity, such as catalysis, chemical sensing and energy conversion [39]. To further analyze the crystallinity of the constituent NPs within the sample, we performed selected-area electron diffraction (SAED). In agreement with XRD and HRTEM results, the SAED pattern in Fig. 1d demonstrates a random orientation of highly crystalline CoO NPs into the pore walls, displaying a sequence of broad Debye–Scherrer diffraction rings with a homogeneous intensity which can be readily assigned to the hexagonal phase of CoO (JCPDS
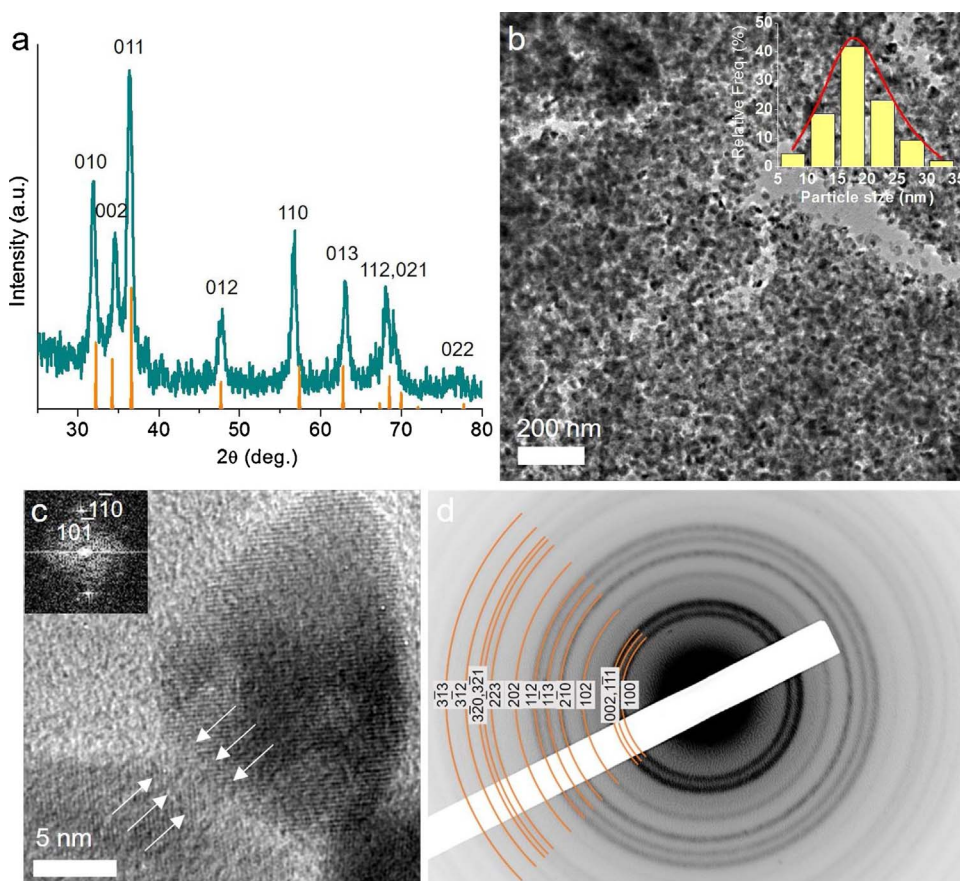
Fig. 1. (a) XRD pattern, (b) typical TEM image (inset: particle size distribution plot), (c) high-resolution TEM (inset: the corresponding FFT pattern) and (d) SEAD pattern for CoO MNAs. In panel a, the standard diffraction lines of hexagonal CoO (JCPDS card no. 48-1719) are also given. The arrows in panel c indicate linking area between adjacent NPs.

card no. 48-1719).

Nitrogen physisorption measurements indicated the mesoporous nature of CoO NP assemblies. Fig. 2 depicts typical adsorption-desorption isotherms and the corresponding pore size distribution plot for the CoO MNAs. The isotherms exhibit a type IV shape accompanied with a H_3 type hysteresis loop, suggesting mesoporous structure with slit-shaped pores. The delayed closure of the hysteresis loop could be associated with potential surface pore-blocking effects. The specific surface area and total pore volume of the CoO MNAs were measured to be 96 $m^2 \, g^{-1}$, according to the Brunauer-Emmett-Teller (BET) method, and 0.14 $cm^3 \, g^{-1}$, respectively. The pore size distribution plot,

obtained from the adsorption branch of isotherms using the non-local density functional theory (NLDFT), shows a quite narrow size distribution with a pore diameter of about 4.8 nm (Fig. 2, inset). Comparatively, random aggregates of CoO NPs (CoO RNAs), which have been prepared by direct mixing of BF_4^--capped CoO NPs in THF without template, possess a lower surface area of 74 $m^2 \, g^{-1}$ and small interstitial voids (ca. 2.3 nm) among the CoO NPs (Fig. 2 and Supporting Fig. S4). These results clearly suggest that the F127 polymer plays an important role in synthesis of CoO MNAs by assisting the self-assembly of colloidal NPs into mesoporous structures.

3.2. Photocatalytic study

3.2.1. Effect of catalyst loading and pH of solution on reaction kinetics

The catalytic activity of as-prepared CoO materials was initially evaluated in photoreduction of aqueous Cr(VI) under UV–vis light irradiation ($\lambda > 360$ nm). First, we optimized the reaction conditions by measuring the Cr(VI) reduction rate for different loadings of the catalyst. As can be seen from Fig. 3a, with increasing catalyst addition, the reduction rate of Cr(VI) is increased until reaching a maximum at $\sim 0.3 \, g \, L^{-1}$. The CoO MNAs concentration-dependent degradation rate of Cr(VI) can be explained by the enhancement of the light absorption by the catalyst's NPs. However, as indicated in Fig. 3a, excess amount of catalyst (more than 0.4 $g \, L^{-1}$) may counter this effect, leading to a slight decrease in Cr(VI) reduction efficiency, presumably due to the light scattering effect from the particles surface [40]. Meanwhile, control experiments have been carried out to demonstrate the photocatalytic nature of the reactions. The results showed that the reduction of Cr(VI) does not take place in the absence of catalyst or light irradiation. The pH of the solution is another critical parameter that influences the photocatalytic reduction of Cr(VI) [41,42]. Fig. 3b depicts that this process is favored for low pH values 1–2, while increasing to
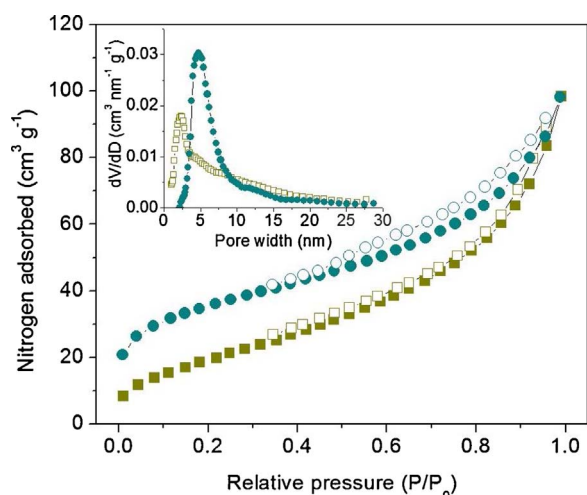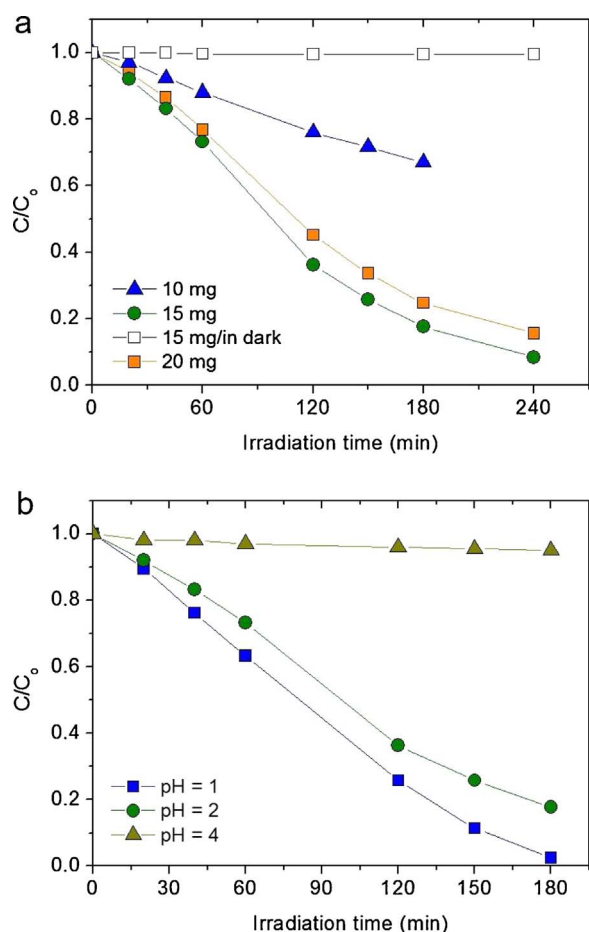

Fig. 2. N_2 adsorption-desorption isotherms at -196 °C and the corresponding NLDFT pore-size distributions of the CoO MNAs (circle symbols) and CoO RNAs (square symbols) materials. The N_2 isotherms of the CoO MNAs are offset by 10 $cm^3 \, g^{-1}$ for clarity.

Fig. 3. Time courses of photocatalytic reduction of Cr(VI) under varying experimental conditions: (a) concentration of catalyst and (b) pH of solution. Reaction conditions: 10–20 mg of CoO MNAs catalyst, 50 mL of 50 ppm Cr(VI) aqueous solution, pH = 1–4, UV–vis light ($\lambda > 360$ nm) irradiation.

Fig. 4. Photocatalytic reduction of aqueous Cr(VI) with CoO MNAs catalyst in the absence and presence (0.4 mg mL^{-1}) of phenol (PhOH) under UV and visible light irradiation. Reaction conditions: 15 mg catalyst, 50 mL of 50 ppm Cr(VI) solution, pH = 2, 20 °C reaction temperature.

pH 4 no apparent Cr(VI) reduction ($\sim 5\%$) was observed after 3 h of irradiation. This is in line with previous studies mentioning that by raising pH of solution from 2 to 4 the conversion of Cr(VI) decreases [43]. It is well known that the predominating species of Cr(VI) at acid pH (pH = 1–2) is $HCrO_4^-$, which are gradually converted to CrO_4^{2-} by increasing pH [44]. Since the $HCrO_4^-$ oxyanions (E^o ($HCrO_4^-/Cr^{3+}$) = 0.86 V) are stronger oxidants than CrO_4^{2-} (E^o (CrO_4^{2-}/Cr_2O_3) = 0.56 V), the electron transfer process to these species is therefore favorable [45]. Note that all potentials reported in this work are referenced against the normal hydrogen electrode (NHE) at pH = 7. In addition, in such high acidic conditions the surface of the CoO catalyst is positively charged favoring the attraction of negatively charged $HCrO_4^-$ complexes (the point of zero charge (pzc) of CoO is reported to be ~ 9.2) [46], thus accelerating the photoreduction of Cr(VI) to Cr(III). In agreement with this assumption, at higher pH the surface is protonated in weaker range and repels chromate anions leading to a significant decrease in photocatalytic reduction rate of Cr(VI).

3.2.2. Photocatalytic reduction of Cr(VI) by the CoO/phenol/UV–vis system

To study the visible light response of CoO MNAs catalyst, we carried out Cr(VI) photocatalytic reduction experiments under irradiation of $\lambda \geq 420$ nm light. As shown in Fig. 4, under visible-light irradiation, the photocatalytic reaction proceeds gradually and nearly 56% of the Cr (VI) is reduced in 4 h. In comparison, when UV–vis light ($\lambda > 360$ nm) was irradiated on CoO mesoporous, the conversion yield reaches 92% at the same period. Recent studies have shown the formation of hot
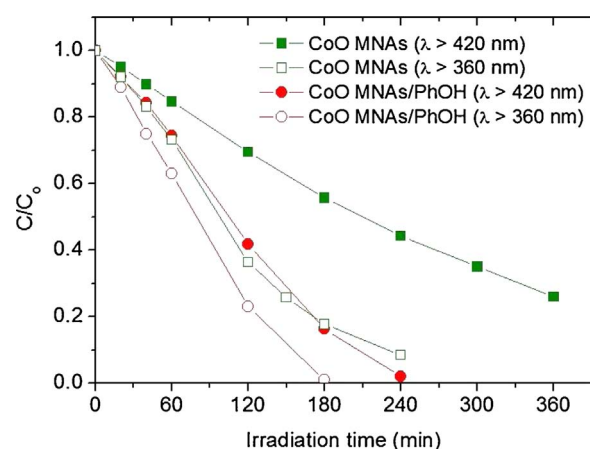
(high-energy) carriers in colloidal semiconductor NPs through above-gap excitation [47,48]. It was suggested that such a high photon-energy pump can facilitate the transfer process of photoinduced hot holes in semiconductors, competing interband charge-carrier transitions [49]. Similarly, the relatively higher efficiency of the CoO MNAs under UV–vis-light irradiation could be potentially attributed to the higher hole transfer yield as a result of the shorter wavelength excitation. In line with this, the apparent quantum yield (AQY) of the Cr(VI) reduction, which is a key metric for the operational efficiency of a photocatalytic system, was estimated to be $\sim 1.61\%$ at $\lambda = 375$ nm and $\sim 0.17\%$ at $\lambda = 440$ nm, assuming all incident photons were absorbed by the catalyst's NPs. Of note, the efficiency of the CoO MNAs catalyst is among the highest reported values of semiconductor photocatalysts that perform Cr(VI) reduction without the combined use of sacrificial donors. For instance, Au/TiO$_2$-Pt nanocomposites showed a maximum AQY of 1.0% at 550 nm [50], CuFe$_2$O$_4$/CdS composites showed a 1.1% AQY at 430 nm [51], and Ba$_2$SnO$_4$ particles exhibited a 0.13% AQY [52] and CuAl$_2$O$_4$/TiO$_2$ heterostructure reached a AQY of 0.11% [53] under polychromatic light. It should be stressed that this photocatalytic activity was obtained by using single-component CoO catalyst and further improvement of its catalytic performance is expected, for instance, when various synthetic methods are utilized to obtain complex heterojunctions with suitable band edge positions (for the efficient separation of the photogenerated charges).

To test the role of photogenerated electrons and holes in catalytic process, UV and visible light photocatalytic Cr(VI) reduction experiments were also carried out in the absence and presence of phenol as a sacrificial hole acceptor. The oxidation of phenol is thermodynamically (~ 0.96 V) [54] and kinetically more favourable than the oxidation of water (0.82 V), and thus often this process can accelerate the overall photocatalytic reaction [40,55]. The high concentration of phenol (10 equiv.) employed in our experiments ensures that the surface of CoO NPs is saturated with excess of phenol. At these conditions, the reaction rate is not diffusion limited and therefore should be independent of phenol concentration (i.e., the hole transfer across the solid/liquid interface is not a diffusion-controlled process). Catalytic results shown in Fig. 4 indicate that addition of 0.4 g L^{-1} of phenol into the Cr(VI) solution (50 ppm) leads to a considerable increase in photoreduction rate under $\lambda \geq 420$ nm illumination, resulting in almost quantitatively ($> 99\%$) conversion of Cr(VI) at 4 h; note that the detection limit of the analysis method is 5 μg L^{-1}. Comparatively, under identical conditions, when the CoO–Cr(VI)–phenol catalytic system was irradiated with UV–vis light, the Cr(VI) reduction reached a moderately higher rate than with visible light. For example, using $\lambda > 360$ nm light, the average reduction rate of $HCrO_4^-$ increased from 5.49 to

7.66 µmol h^{-1}. This different behavior could be tentatively related with the transfer rate of hot carriers generating from high photon-energy excitation; such hot carriers may have little effect on the hole transfer process from CoO NPs to phenol, but play a more prominent role in photooxidation of water. Unlike water, phenol seems to enable efficient utilization of surface reaching holes (hot and relaxed holes), leading to an improvement of the oxidation efficiency. This means that the high propensity for oxidation of phenol can diminish the differences in catalytic activity that may arise from the change in photon energy of the radiation and the overall reaction can readily proceed at a faster rate. The conversion of phenol to diphenyl oxide, and thus its direct participation in the photocatalytic process as an electron donor, was confirmed by GC–MS analysis of the reaction products (see Fig. S5). Taken together, it is obvious that oxidation process by CoO surface holes is the reaction rate-controlled step in the CoO–Cr(VI) catalytic system. Note that the synergistic degradation of organic pollutants such as phenol by Cr(VI) reduction is of vital importance for practical applications. Apart from chromium, groundwater contains also other pollutant byproducts such as colorless organic chemicals and recalcitrant dyes [43], which their decontamination is a major concern [56,57]. This study clearly suggests that the photocatalytic reduction of Cr(VI) and oxidation of phenol are collaborative over mesoporous CoO NP assemblies and this process can enhance the photoreduction effect.

3.2.3. Effects of materials morphology on the photoactivity of CoO NPs

In addition to the oxidation kinetics at the CoO/solution interface, morphological effects may also contribute to the high photoactivity of CoO MNAs. This can be investigated by comparing photocatalytic data for Cr(VI) reduction by individual CoO NPs and random aggregates of CoO NPs (CoO RNAs). Results shown in Fig. 5a indicate that these materials afforded a considerably lower catalytic performance than that obtained for Cr(VI) reduction at mesoporous CoO NP assemblies. Assuming that the reaction rate is proportional to the concentration of Cr (VI), the photocatalytic reaction can be investigated by the first-order kinetics of Langmuir-Hinshelwood model. Thus, the kinetic data obtained from analysis of the temporal evolution of Cr(VI) concentration using the first-order reaction rate (Eq. (2)) reveal that the reaction proceeds at a lower rate over isolated CoO NPs ($k = 2.7 \times 10^{-3}$ min^{-1}) and random aggregates CoO RNAs ($k = 0.9 \times 10^{-3}$ min^{-1}) than mesoporous CoO assemblies ($k = 4.9 \times 10^{-3}$ min^{-1}) under identical conditions (Fig. S6).

$$\ln(C_o/C_t) = kt \qquad (2)$$

where, C_o and C_t is the concentration of Cr(VI) at initial time and time t, respectively, and k is the apparent reaction rate constant.

Presumably, under the reaction conditions, the BF$_4^-$ ligands anchored on the CoO NPs surface are not sufficient to prevent agglomeration of the colloidal particles, and thus a deterioration of the catalytic performance was observed. On the other hand, the CoO RNAs although have an adequate surface area (74 m^2 g^{-1}), contains a random distribution of small-sized pores between the NPs that possible results in slow diffusion kinetics of Cr(VI) ions. Therefore, from these results, it can be inferred that the material's surface area and pore volume play an important role in the reduction rate of Cr(VI).

Of particular note, mesoporous assemblies of cubic CoO NPs (denoted as c-CoO MNAs), which were obtained by polymer-templated self-assembly of cubic structured CoO NPs [34], showed a lower UV–vis-light Cr(VI) reduction activity (~51% Cr(VI) reduction ratio at 4 h; $k = 1.9 \times 10^{-3}$ min^{-1}, see Fig. S6) than the corresponding CoO MNAs catalyst with hexagonal phased CoO NPs. Similar to CoO MNAs, the c-CoO MNAs material exhibited a BET surface area as high as 134 m^2 g^{-1} and a pore size of 4.4 nm (Fig. S7). We believe that the difference in activity originates from the structural stability and the hole oxidation kinetics in CoO NPs. It is known that the crystal structure of cubic CoO (space group *Fmm*) is composed of CoO$_6$ octahedra,
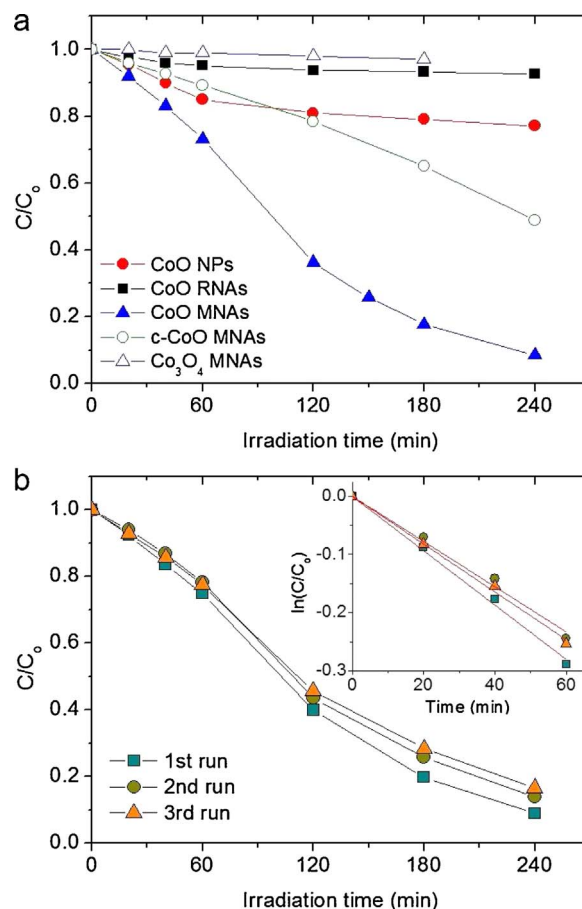

Fig. 5. (a) Photocatalytic reduction of Cr(VI) over different photocatalysts. (b) Recycling study of the CoO MNAs catalyst (Inset: kinetic plots of pseudo-first-order reaction rates. The red lines are fit to the data). All photocatalytic reactions were performed as follows: 15 mg of catalyst was dispersed in a 50 mL aqeous solution containing 50 ppm Cr(VI), under UV–vis light (λ > 360 nm) irradiation. (For interpretation of the references to color in this figure legend, the reader is referred to the web version of this article.)

whereas that of hexagonal CoO (space group $P6_3mc$) contains tetrahedral CoO$_4$ units. The high stability and thus low reactivity of Co$^{\delta+}$–O$^{\delta-}$ bonds may be related to the higher crystal field stabilization energy (CFSE) of the high-spin d^7 Co(II) centers of cubic CoO ($-4/5\Delta_o$ *versus* $-6/5\Delta_t \approx -8/15\Delta_o$ for tetrahedral d^7 Co(II) ions). This means that although cubic CoO is a thermodynamically more stable phase than hexagonal CoO structure, it is less active for the generation of ·OH free radicals by hole oxidation of surface-bound −OH groups or absorbed water molecules. The above argument is also in accordance with the monitoring of the ·OH production rate with fluorescence spectroscopy, where the results corroborated to the lower oxidation kinetics of cubic CoO NPs (see below).
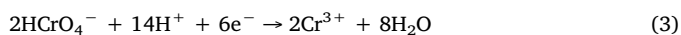
We also tested the Cr(VI) reduction in water using mesoporous Co$_3$O$_4$ NP aggregates (Co$_3$O$_4$ MNAs), and a negligible UV–vis-light Cr (VI) reduction activity (~3% Cr(VI) reduction ratio) was detected, even after 3 h of illumination (see Fig. 5a). This new material was obtained by annealing of the CoO NPs/F127 composite in air at elevated temperature (350 °C). XRD pattern confirmed that the thermally converted sample is pure-phase cubic spinel Co$_3$O$_4$, while N$_2$ physisorption isotherms revealed an open porous structure (Fig. S8); the Co$_3$O$_4$ MNAs exhibit a BET surface area of 62 m^2 g^{-1} and a total pore volume of 0.15 cm^3 g^{-1}. These data clearly suggest that single-component Co$_3$O$_4$ is unsatisfactory catalyst for the simultaneous reduction of Cr(VI) and oxidation of water, although it has small grain size composition (ca. 12 nm based on Scherrer analysis) and large internal surface area, similar to those of CoO MNAs. These findings are in agreement with

earlier studies that involve Co_3O_4 NP-based photocatalysts [58]. Therefore, taken together, the catalytic results support that, apart from the surface area, the crystal phase of CoO plays a key role by promoting the oxidation half-reaction by the photoinduced holes and contributing to the high Cr(VI) reduction activity.
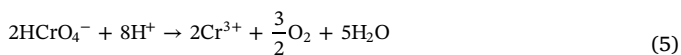
We have further studied the stability and reusability of the catalyst by conducting a series of Cr(VI) photoreduction experiments. The catalyst was recovered from the reaction mixture by simply filtration and re-dispersed in a fresh Cr(VI) aqueous solution. As illustrated in Fig. 5b, the CoO MNAs show an adequate cyclic stability in the examined conditions, retaining about 92% of the initial activity after three consecutive 4-h photocatalytic runs ($k^1 = 4.6 \times 10^{-3}$ min^{-1}; $k^2 = 4.0 \times 10^{-3}$ min^{-1}; $k^3 = 4.1 \times 10^{-3}$ min^{-1}). This loss might be partly related to the mass loss of the photocatalyst during each isolation step. XRD and N_2 physisorption measurements indicated no crystal decomposition and structural collapse or obvious shrinkage for the retrieved CoO MNAs catalyst (Fig. S9). Moreover, X-ray photoelectron spectroscopy (XPS) measurements further confirm the CoO chemical nature of the catalysts before and after catalytic test, showing Co $2p_{3/2}$ core-level signal with binding energy at 781.2 eV. This binding energy as well as the broad satellite feature appeared at about 5.5 eV higher binding energy from the main peak are characteristic of the Co(II) oxidation state [59], see Fig. S10.

3.3. Reaction mechanism of photocatalytic reduction of aqueous Cr(VI) under UV–vis light

To better understand and interpret our catalytic findings, photocatalytic experiments were carried out in an air-tight cell with CoO MNAs catalyst suspended in a 50 ppm Cr(VI) aqueous solution, and the headspace content of the cell was analyzed by a gas chromatography (GC) equipped with a thermal conduction detector. Before irradiation, the solution was purged with argon until oxygen was fully removed. The results directly demonstrate that CoO MNAs is active in O_2 evolution reaction under UV–vis light irradiation, showing an average O_2-production rate of ∼1.9 μmol h^{-1} (Fig. 6a). To further verified the generation of oxygen during the catalytic reaction, we performed on-line mass spectrometry measurements of photocatalytic oxygen evolution. In particular, we conducted the same photocatalytic test as above in a vacuum-tight cell with CoO MNAs catalyst and the generated oxygen gas was monitored in situ with a mass spectrometer (Hiden HPR-20 QIC gas analyzer). Fig. 6b presences the transient photocatalytic O_2 evolution response of CoO MNAs under intermittent UV–vis light irradiation. It can be seen that the production of oxygen increased with time under light irradiation, while no oxygen evolution was observed when the reaction was conducted in the dark. This observation clearly confirms that the photocatalytic reduction of Cr(VI) occurs by the spontaneous photooxidation of water at the CoO/aqueous interface. Thus, the main processes of the photocatalytic reaction at acid pH solution can be described as follows:

$$2HCrO_4^- + 14H^+ + 6e^- \rightarrow 2Cr^{3+} + 8H_2O \tag{3}$$

$$3H_2O + 6h^+ \rightarrow \frac{3}{2}O_2 + 6H^+ \tag{4}$$

Consequently, the overall reaction can be described by Eq. (5).

$$2HCrO_4^- + 8H^+ \rightarrow 2Cr^{3+} + \frac{3}{2}O_2 + 5H_2O \tag{5}$$

It is noteworthy that oxygen is produced at a lower rate (∼1.9 μmol h^{-1}) with the expected value according to the stoichiometry of $HCrO_4^-$ reduction; we obtained a ∼5.75 μmol h^{-1} of $HCrO_4^-$ reduction rate under UV–vis-light irradiation which, based on Eq. (5), consists in an O_2 evolution rate of about 4.3 μmol h^{-1}. We ascribe this difference to the oxidation of hydroxyl groups or absorbed water molecules at the surface into hydroxyl radicals (·OH) by photogenerated
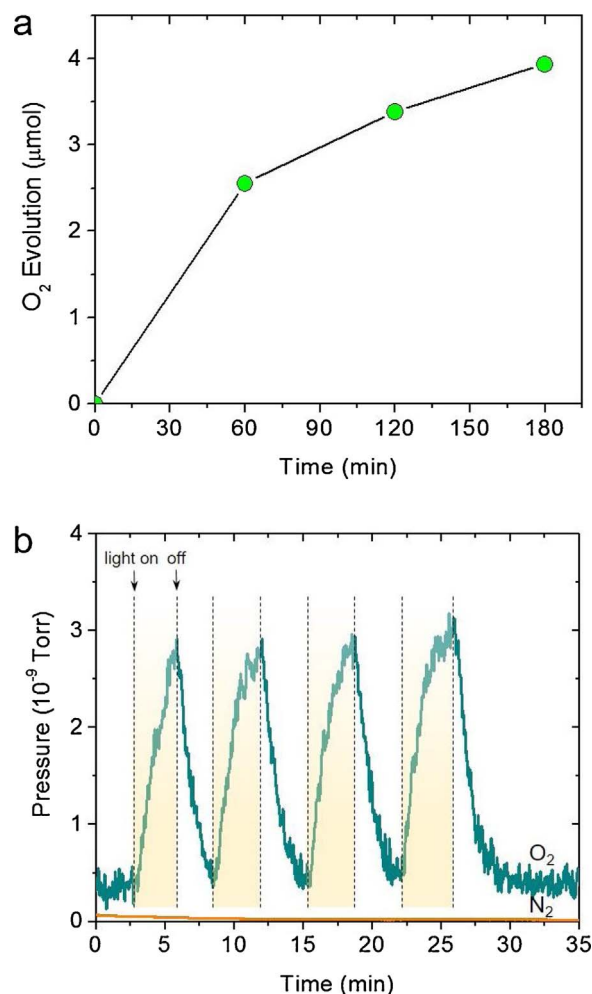

Fig. 6. (a) Time course for photocatalytic O_2 evolution and (b) O_2 evolution transient with light on/off for CoO MNAs catalyst under UV–vis light ($\lambda > 360$ nm) irradiation.

holes:

$$Co–OH_s + h^+ \rightarrow [Co^+ \cdot OH]_s \tag{6}$$

$$H_2O_{abs} + h^+ \rightarrow \cdot OH + H^+ \tag{7}$$

An incontestable qualification for the formation of ·OH radicals during the photoreduction of Cr(VI) was obtained by the fluorescence probe method, utilizing coumarin in the experiment. Coumarin is an effective probe molecule for monitoring hydroxyl radical in solutions, as it can readily react with ·OH producing umbelliferone, which under excitation at 332 nm show a characteristic fluorescence signal at 455 nm wavelength [60]. Fig. 7a presents the respective fluorescence spectra obtained at certain time intervals during the course of the reaction. It is shown the gradually decrease of coumarin and increase of umbelliferone emission over 3 h irradiation, recommending the existence of hydroxyl radicals in the solution. We suspect that an electron-transfer-type oxidation of either surface Co—OH (or Co—O—Co) groups or adsorbed water molecules by photogenerated holes in CoO NPs could be responsible for the formation of hydroxyl radicals in the solution. In general, the oxidation rate of hydroxyl radicals which is a one-electron-transfer process (Eqs. (6) and (7)) is much faster than the rate of the oxygen photoevolution reaction, i.e. $2H_2O \rightarrow O_2 + 4H^+ + 4e^-$. Comparatively, we also conducted the same experiment using the c-CoO MNAs as a catalyst. As revealed in Figs. 7b and c, the c-CoO MNAs catalyst exhibits an approximately 2.7-fold lower production rate of ·OH radicals, which is defined by the ratio of intensity between umbelliferone and coumarin, than that of CoO MNAs at identical
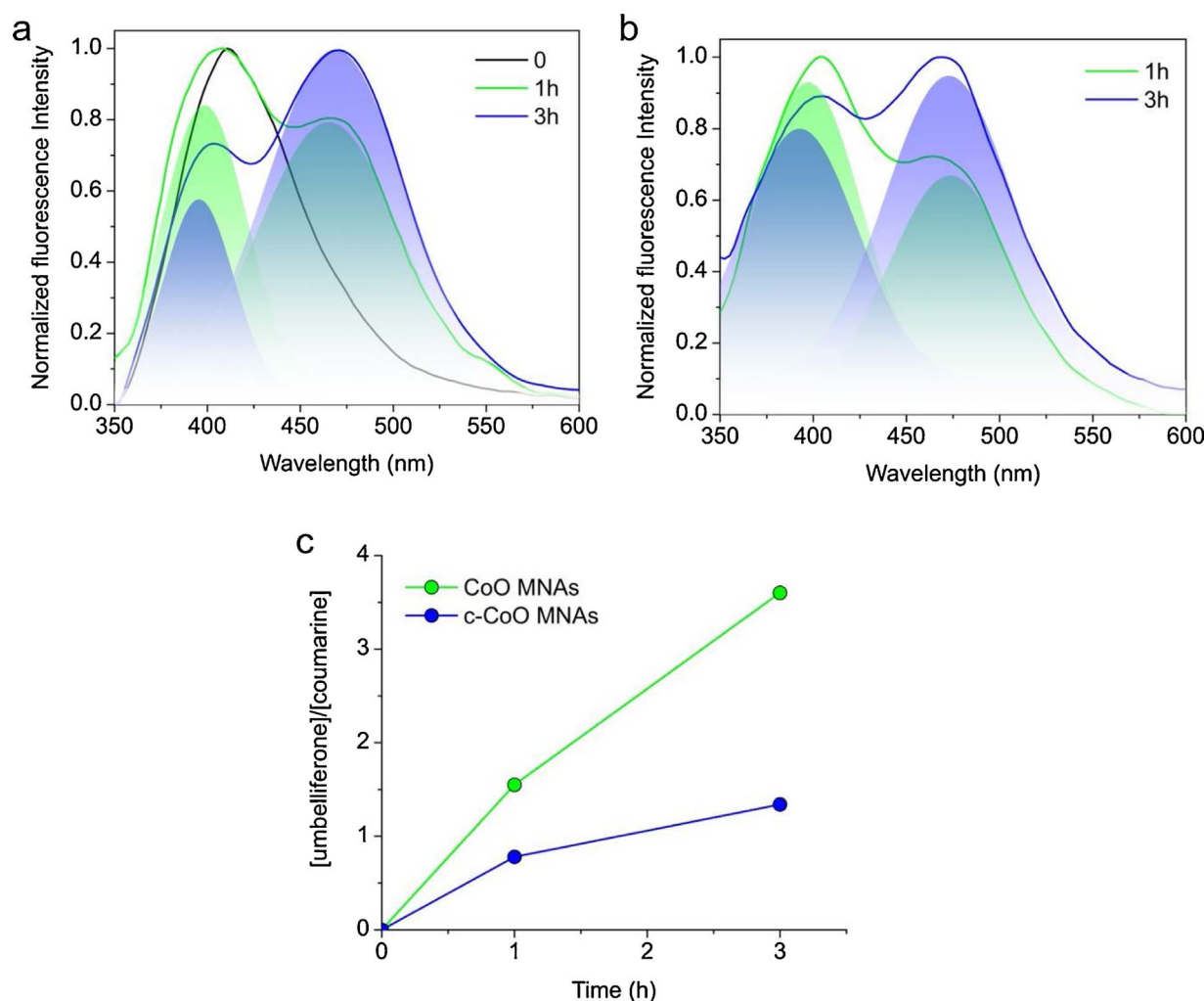
Fig. 7. Time course of fluorescence spectra of the coumarin in water for (a) CoO MNAs and (b) c-CoO MNAs catalyst. The emission peak seen at ~395 nm corresponds to the coumarin, while the peak at ~455 nm arises from umbelliferone. In pane a, the fluorescence spectrum of coumarin (t = 0) is also given. Reaction conditions: 15 mg catalyst, 50 mL of 50 ppm Cr (VI), 10 mM coumarin, pH = 2, 20 °C, UV–vis light (λ > 360 nm). Fluorescence emission spectra obtained with an excitation wavelength of 332 nm. (c) The integrated fluorescence intensity ratio of the umbelliferone emission at ~455 nm to coumarin emission at ~398 nm for CoO MNAs and c-CoO MNAs catalysts.

conditions. The lower OH− oxidation kinetics for c-CoO MNAs could be attributed to the most stable Co−OH bond of cubic CoO structure, which impedes the formation of hydroxyl radicals and subsequently conversion to umbelliferone. These results suggest that the favorable oxidation of surface hydroxyl groups by surface-trapped holes (instead of the sluggish water dissociation step) plays a critical role in accelerating the oxidation rate, resulting in a rapid generation of ·OH radicals. The hexagonal CoO NPs behave similarly in this respect, and this is reflected in high activity towards Cr(VI) reduction. However, more experimentation is need in order to elucidate the crystal-phase-related catalytic properties of the CoO NPs.

The electronic band structure and optical transitions in CoO NPs were investigated by combining electrochemical impedance (EIS) and UV–vis spectroscopy. Fig. 8a displays the Mott-Schottky plot and the corresponding fit of the linear portion of inverse square of capacitance ($1/C^2$) of the space charge region *versus* electrode potential (*E*) for the CoO MNAs catalyst. We used the extrapolation to $1/C^2 = 0$ to determine the flat-band potential (E_{FB}) of CoO MNAs, which was calculated to be −0.04 V *vs* NHE (pH = 7). Moreover, the electron donor density (N_D) of CoO is 4.02×10^{16} cm^{-3}, as determined by the slope of the $1/C^2$ *versus E* plot. Noted that the positive slope of the Mott-Schottky plot indicates that CoO MNAs shows n-type behavior. We tentative ascribe the *n*-type conductivity of our CoO sample to intrinsic point defects such as oxygen vacancies, which have been found to be

responsible for n-doping in similar CoO materials [61]. The VB maximum for CoO MNAs is thus estimated at 2.57 V *vs* NHE (pH = 7) from the difference of E_{FB} and energy band gap (E_g) of the semiconductor. The E_g value of CoO MNAs, which was determined from optical absorption data using the Tauc equation, was found to be ~2.61 eV (Fig. 8a, inset). Comparatively, the calculated energy gap of CoO RNAs was estimated to be slightly lower at ~2.56 eV, as expected due to smaller pore structure.

In light of these findings, a potential photocatalytic mechanism for the reduction of Cr(VI) has been proposed, as shown in Fig. 8b. In short, under UV or visible light irradiation, CoO NPs get excited and generate electron-hole pairs. The favourable thermodynamic conditions of the band structure drive the transfer of photoexcited electrons from the CB to the Cr(VI) species; the CB edge of CoO NPs lies above the redox potential of the HCrO$_4^-$/Cr^{3+} couple (0.86 V) [62]. Meanwhile, since the VB level of CoO NPs is more positive than the O$_2$/H$_2$O redox potential (0.82 V), the photogenerated holes can oxidize water, producing oxygen. In addition, during the course of irradiation, a fraction of surface-trapped holes (Lewis acids) may be also transferred to the hydroxyl groups or adsorbed water molecules (Lewis bases), causing the formation of ·OH radicals; the redox potentials of ·OH/OH$^-$ (E^o = 1.58 V) [63] and ·OH/H$_2$O (E^o = 1.92 V) [64] pairs are above the VB edge of CoO NPs (2.57 V) and they oxidation is a viable possibility. The presence of ·OH radicals in the solution was evidenced by

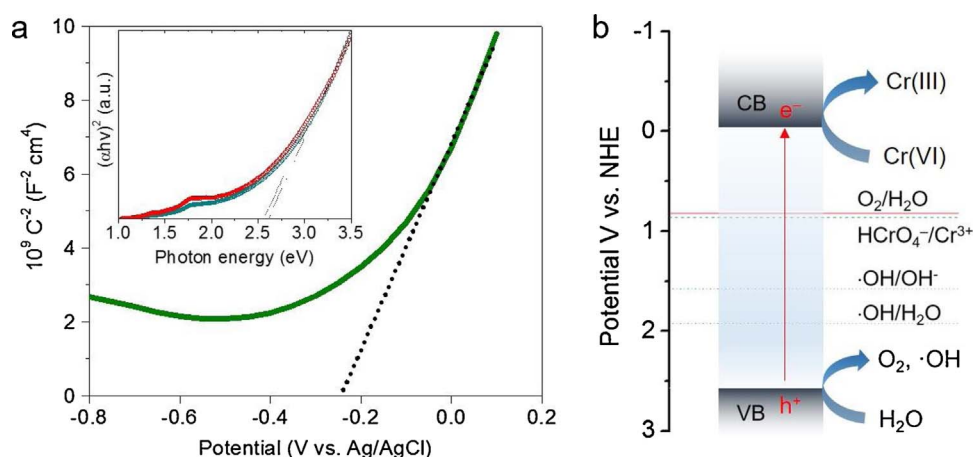**Fig. 8.** (a) Mott-Schottky plot of the CoO MNAs. Inset: Tauc plots [$(\alpha h v)^2$ *vs* photon energy, where α is the absorption coefficient, h is the Planck's constant, and v is the light frequency] derived from UV–vis optical absorption data for mesoporous assemblies (CoO MNAs, green line) and random aggregates (CoO RNAs, red line) of CoO NPs. (b) Energy band diagram and possible reaction mechanism for the photoreduction of Cr(VI) over CoO MNAs catalyst.

fluorescence spectroscopy. This observation is in line with previous studies that report the phase transformation of hexagonal CoO to β-Co(OH)$_2$ by hydration of the CoO surface [65]. Such cobalt hydroxide species on the surface of CoO NPs may possess advantages for the formation of hydroxyl radicals during the photocatalytic reaction. We have to note that the resultant ·OH radicals also have the ability to recombine with each other, producing H$_2$O$_2$, which may further be oxidized by the holes to dioxygen [66]. Meanwhile, the *in situ* generated ·OH radicals may be also considered as a primary oxidant for the photocatalytic degradation of organic pollutants at the CoO surface, such as phenol, facilitating the charge carrier separation through the fast hole transfer kinetics and thus accelerating the overall Cr(VI) reduction process.

4. Conclusions

In summary, high-surface-area NP-linked mesoporous CoO networks were successfully synthesized *via* a polymer-assisted co-assembly of colloidal CoO NPs and amphiphilic block-copolymer aggregates. The as-prepared materials show an open-pore structure consisting of tightly bonded NPs with an average diameter of 18 nm and manifest excellent photocatalytic performance for reduction of Cr(VI) in aqueous solutions. Our results indicated the that the unprecedented photocatalytic activity of CoO MNAs catalyst is presumably a result of the combined effect of accessible pore volume, appropriate band edge positions and specific reactivity of the crystal phase. Control catalytic experiments coupled with on-line mass spectrometry and fluorescence spectroscopy confirmed that the Cr(VI) reduction reaction proceeds simultaneously with the competitive formation of molecular oxygen and hydroxyl radicals at the CoO surface. Indeed, hexagonal CoO NPs favor the oxidation half reaction through a localized-hole-mediated ·OH radical production mechanism, accelerating the reduction of Cr(VI). The remarkable activity and durability of the CoO MNAs implies the great possibility of implementing this new catalyst into a realistic Cr(VI) detoxification of contaminated water.

Acknowledgements

Appendix A. Supplementary data

Supplementary data associated with this article can be found, in the online version, at http://dx.doi.org/10.1016/j.apcatb.2017.09.064.

References

[1] A.D. Bokare, W. Choi, J. Environ. Sci. Technol. 44 (2010) 7232–7237.
[2] G. Gollavelli, C.-C. Chang, Y.-C. Ling, ACS Sustain. Chem. Eng. 1 (2013) 462–472.
[3] S.A. Katz, H.J. Salem, Appl. Toxicol. 13 (1993) 217–224.
[4] S. Peyrav, R. Zahiri, K.M. Hersini, J. Chem. Health Risks 1 (2011) 11–18.
[5] United States Environmental Protection Agency (U.S. EPA), IRIS Toxicological Review of Hexavalent Chromium (External Review Draft), U.S. Environmental Protection Agency, Washington, DC, 2010 EPA/635/R-10/004A.
[6] C.E. Barrera-Diaz, V. Lugo-Lugo, B. Bilyeu, J. Hazard. Mater. 223–224 (2012) 1–12.
[7] Y. Tian, L. Huang, X. Zhou, C. Wu, J. Hazard. Mater. 225–226 (2012) 15–20.
[8] A. Lu, S. Zhong, J. Chen, J. Shi, J. Tang, X. Lu, Environ. Sci. Technol. 40 (2006) 3064–3069.
[9] S.W. Hu, L.W. Yang, Y. Tian, X.L. Wei, J.W. Ding, J.X. Zhong, P.K. Chu, Appl. Catal. B: Environ. 163 (2015) 611–622.
[10] S. Cao, J. Low, J. Yu, M. Jaroniec, Adv. Mater. 27 (2015) 2150–2176.
[11] B. Sun, E.P. Reddy, P.G. Smirniotis, Environ. Sci. Technol. 39 (2005) 6251–6259.
[12] Y. Li, W. Cui, L. Liu, R. Zong, W. Yao, Y. Liang, Y. Zhu, Appl. Catal. B: Environ. 199 (2016) 412–423.
[13] J. Shang, W. Hao, X. Lv, T. Wang, X. Wang, Y. Du, S. Dou, T. Xie, D. Wang, J. Wang, ACS Catal. 4 (2014) 954–961.
[14] Q. Cheng, C. Wang, K. Doudrick, C.K. Chan, Appl. Catal. B: Environ. 740 (2015) 176–177.
[15] Y.C. Zhang, J. Li, M. Zhang, D.D. Dionysiou, Environ. Sci. Technol. 45 (2011) 9324–9331.
[16] W. Yang, L. Zhang, Y. Hu, Y. Zhong, H.B. Wu, X.W. Lou, Angew. Chem. Int. Ed. 51 (2012) 11501–11504.
[17] X. Liu, L. Pan, T. Lv, G. Zhu, Z. Suna, C. Sun, Chem. Commun. 47 (2011) 11984–11986.
[18] H. Abdullah, D.-H. Kuo, ACS Appl. Mater. Interfaces 7 (2015) 26941–26951.
[19] G. Dong, L. Zhang, J. Phys. Chem. C 117 (2013) 4062–4068.
[20] G. Chen, M. Sun, Q. Wei, Z. Ma, B. Du, Appl. Catal. B: Environ. 125 (2012) 282–287.
[21] R. Nakamura, T. Okamura, N. Ohashi, A. Imanishi, Y. Nakato, J. Am. Chem. Soc. 127 (2005) 12975–12983.
[22] H. Jiang, R.I. Gomez-Abal, P. Rinke, M. Scheffler, Phys. Rev. B: Condens. Matter Mater. Phys. 82 (2010) 045108.
[23] W.-Y. Li, L.-N. Xu, J. Chen, Adv. Funct. Mater. 15 (2005) 851–857.
[24] P. Poizot, S. Laruelle, S. Grugeon, L. Dupont, J.-M. Tarascon, Nature 407 (2000) 496–499.
[25] X. He, W. Zhong, S. Yan, C. Liu, H. Shi, C.-T. Au, Y. Du, J. Phys. Chem. C 118 (2014) 13898–13903.
[26] K.M. Nam, Y.C. Choi, S.C. Jung, Y.-I. Kim, M.R. Jo, S.H. Park, Y.-M. Kang, Y.-K. Han, J.T. Park, Nanoscale 4 (2012) 473–477.
[27] G. Margaris, K.N. Trohidou, J. Nogués, Adv. Mater. 24 (2012) 4331–4336.
[28] L. Liao, Q. Zhang, Z. Su, Z. Zhao, Y. Wang, Y. Li, X. Lu, D. Wei, G. Feng, Q. Yu, X. Cai, J. Zhao, Z. Ren, H. Fang, F. Robles-Hernandez, S. Baldelli, J. Bao, Nat. Nanotechnol. 9 (2014) 69–73.
[29] I.T. Papadas, I. Vamvasakis, I. Tamiolakis, G.S. Armatas, Chem. Mater. 28 (2016) 2886–2896.
[30] I. Tamiolakis, I.T. Papadas, K. Spyridopoulos, G.S. Armatas, RSC Adv. 6 (2016) 54848–54855.
[31] I.T. Papadas, S. Fountoulaki, I.N. Lykakis, G.S. Armatas, Chem. Eur. J. 22 (2016) 4600–4607.
[32] I.T. Papadas, K.S. Subrahmanyam, M.G. Kanatzidis, G.S. Armatas, Nanoscale 7 (2015) 5737–5743.
[33] E. Skliri, S. Papadogiorgakis, I.N. Lykakis, G.S. Armatas, ChemPlusChem 82 (2017) 136–143.
[34] W.S. Seo, J.H. Shim, S.J. Oh, E.K. Lee, N.H. Hur, J.T. Park, J. Am. Chem. Soc. 127 (2005) 6188–6189.
[35] A. Dong, X. Ye, J. Chen, Y. Kang, T. Gordon, J.M. Kikkawa, C.B. Murray, J. Am. Chem. Soc. 133 (2011) 998–1006.
[36] S. Brunauer, L.S. Deming, W.E. Deming, E. Teller, J. Am. Chem. Soc. 62 (1940)

1723–1732.

[37] P.I. Ravikovitch, D. Wei, W.T. Chueh, G.L. Haller, A.V. Neimark, J. Phys. Chem. B 101 (1997) 3671–3679.
[38] P. Kubelka, J. Opt. Soc. Am. 38 (1948) 448–457.
[39] F.E. Osterloh, Top. Curr. Chem. 371 (2016) 105–142.
[40] P. Mohapatra, S.K. Samantaray, K. Parida, J. Photochem. Photobiol. A: Chem. 170 (2005) 189–194.
[41] A. Idris, N. Hassan, R. Rashid, A.-F. Ngomsik, J. Hazard. Mater. 186 (2011) 629–635.
[42] A. Idris, N. Hassan, N.S.M. Ismail, E. Misran, N.M. Yusof, A.-F. Ngomsik, A. Bee, Water Res. 44 (2010) 1683–1688.
[43] Q. Wang, X. Shi, E. Liu, J.C. Crittenden, X. Ma, Y. Zhang, Y. Cong, J. Hazard. Mater. 317 (2016) 8–16.
[44] R.M. Cespón-Romero, M.C. Yebra-Biurrun, M.P. Bermejo-Barrera, Anal. Chim. Acta 327 (1996) 37–45.
[45] A.D. Bokare, W. Choi, Environ. Sci. Technol. 44 (2010) 7232–7237.
[46] M. Kosmulski, J. Colloid Interface Sci. 426 (2014) 209–212.
[47] G. Grancini, M. Maiuri, D. Fazzi, A. Petrozza, H.J. Egelhaaf, D. Brida, G. Cerullo, G. Lanzani, Nat. Mater. 12 (2013) 29–33.
[48] S.D. Dimitrov, A.A. Bakulin, C.B. Nielsen, B.C. Schroeder, J.P. Du, H. Bronstein, I. McCulloch, R.H. Friend, J.R. Durrant, J. Am. Chem. Soc. 134 (2012) 18189–18192.
[49] W.A. Tisdale, K.J. Williams, B.A. Timp, D.J. Norris, E.S. Aydil, X.Y. Zhu, Science 328 (2010) 1543–1547.
[50] A. Tanaka, K. Nakanishi, R. Hamada, K. Hashimoto, H. Kominami, ACS Catal. 3 (2013) 1886–1891.

[51] N. Nasrallah, M. Kebir, Z. Koudri, M. Trari, J. Hazard. Mater. 185 (2011) 1398–1404.
[52] S. Omeiri, N. Allalou, R. Gharib, Y. Gabès, Y. Bessekhouad, M. Trari, Theor. Exp. Chem. 49 (2013) 298–303.
[53] R. Gherbia, N. Nasrallaha, A. Amraneb, R. Maachia, M. Trari, J. Hazard. Mater. 186 (2011) 1124–1130.
[54] C. Li, M.Z. Hoffman, J. Phys. Chem. B 103 (1999) 6653–6656.
[55] L. Shen, W. Wu, R. Liang, R. Lin, L. Wu, Nanoscale 5 (2013) 9374–9382.
[56] C. Mu, Y. Zhang, W. Cui, Y. Liang, Y. Zhu, Appl. Catal. B: Environ. 212 (2017) 41–49.
[57] Y. Liang, S. Lin, L. Liu, J. Hu, W. Cui, Appl. Catal. B: Environ. 164 (2015) 192–203.
[58] Y. Hao, F. Li, J. Zhao, R. Liu, X. Wang, Y. Li, Y. Liu, Dalton Trans. 45 (2016) 2444–2453.
[59] M.C. Biesinger, B.P. Payne, A.P. Grosvenor, L.W.M. Lau, A.R. Gerson, R.S.C. Smart, Appl. Surf. Sci. 257 (2011) 2717–2730.
[60] Y. Nakabayashi, Y. Nosaka, J. Phys. Chem. C 117 (2013) 23832–23839.
[61] B.D. Craig, Properties of corrosive films, Fundamental Aspects of Corrosion Films in Corrosion Science, Springer Science, New York, 1991 p. 47.
[62] J. Wang, K. Ashley, D. Marlow, E.C. England, G. Carlton, Anal. Chem. 71 (1999) 1027–1032.
[63] S. Kim, W. Choi, Environ. Sci. Technol. 36 (2002) 2019–2025.
[64] A. Fujishima, X.T. Zhang, C. R. Chim. 9 (2006) 750–760.
[65] K.Y. Jang, G. Park, K.H. Oh, J.H. Seo, K.M. Nam, Chem. Commun. 53 (2017) 4120–4123.
[66] A.P. Salvador, C. Gutiérrez, J. Phys. Chem. 88 (1984) 3696–3698.